Amphicharge-Storable Pyropolymers Containing Multitiered Nanopores

Na Rae Kim, Sang Moon Lee, Min Wook Kim, Hyeon Ji Yoon, Won G. Hong, Hae Jin Kim, Hyoung Jin Choi, Hyoung-Joon Jin, and Young Soo Yun**

In this study, hierarchically nanoporous pyropolymers (HN-PPs) including numerous redox-active heteroatoms are fabricated from polyaniline nanotubes by heating with KOH. In the large operating voltage range 1.0–4.8 V versus Li^+/Li, HN-PPs store amphicharges by a pseudocapacitive manner of Li-ion (mainly <3.0 V) and electrochemical double layer formation of anion (primarily >3.0 V). Through these surface-driven charge storage behaviors, HN-PPs achieve a significantly high specific capacity of ≈460 mA h g^{-1} at 0.5 A g^{-1}, maintaining specific capacities of 140 mA h g^{-1} at a high specific current of 30 A g^{-1} and 305 mA h g^{-1} after 2000 cycles at 3 A g^{-1}. Furthermore, asymmetric energy storage devices based on HN-PPs deliver a high specific energy of 265 W h kg^{-1} and high specific power of 5081 W kg^{-1} with long-term cycling performance.

Energy storage devices (ESDs) have been developing rapidly during the 21st century, as a result of modern society's concern with the use of fossil fuels, over issues such as environmental pollution, emission of greenhouse gases, and resource depletion.[1,2] A key research focus is on realizing eco-friendly and efficient ESDs which are not made of expensive components and have simple configurations.[1,2] Many different types of ESDs, such as metal–air/S batteries,[3–6] Na/K/Al/Mg-ion batteries,[7–11] redox flow batteries,[12,13] supercapacitors,[14,15] and various hybrids[12,16] have been reported, including the well-known Li-ion batteries. Among these, supercapacitors can deliver the highest power and have the longest cycling life as a result of their charge storage mechanism based on physisorption.[14,15] In particular, it was reported that nanopores increase charge storage efficiency by preventing overscreening and by confining the charges geometrically, in comparison to planar electrodes.[17–19] Nevertheless, the kinetic properties with nanometer-sized fine pores are not limited by geometry because of the fast solvation/desolvation dynamic motion of charges and their superionic phenomena.[20,21] Hence, nanoporous carbon-based electrode materials (CEMs) with high specific surface area are a strong candidate to achieve high electrochemical double layer (EDL) capacitance. At the same time, there is another surface-induced charge storage mechanism in CEMs besides the EDL mechanism, which sometimes surpasses the specific EDL capacitance.[22–26] Lee et al. reported Li-ion storage performance of oxygen functional groups on the surface of carbon nanotubes, which delivered a high reversible capacity of ≈200 mA h g^{-1} and a power capability reaching 100 kW kg^{-1}.[22] Presence of oxygen groups plays a key role in the pseudocapacitive behaviors;[23] nitrogen atoms doped into a hexagonal carbon structure (by substituting for carbon atoms) can also enhance specific capacity by improving electrical conductivity with electron-doping.[24,25] It was reported that heteroatom pairs, such as oxygen and nitrogen, on the edge site of the hexagonal carbon structures could store Li-ions in the cathodic voltage region through their synergistic behaviors,[24] indicating that the introduction of more heteroatoms on the edge sites could result in more charge being stored. In contrast, heteroatoms on the basal plane of the hexagonal carbon structures could break the conjugated carbon bonding, deteriorating electrical conductivities of the hexagonal carbon structures. In addition, intrinsic edge defects and pseudo-edge sites of hexagonal carbon structures are possible redox hosts.[7,24,26] Hence, the carbon textural properties and heteroatoms configurations have a key role in the pseudocapacitive charge storage. If these redox-active sites are exposed and in direct contact with an electrolyte, no solid-state ion diffusion is required for a Faradaic reaction, and high energy and high power characteristics result. Therefore, hierarchical nanoporous carbon-based structures, composed of multimodal nanopores and numerous surface heteroatoms, can be an optimal architecture for surface-induced charge storage that is based on both redox reactions and EDL capacitance.

Pyropolymers are a type of carbon-based material fabricated from polymer precursors by low temperature pyrolysis (below 1000 °C). They are composed of numerous hexagonal carbon basic-structural-units (BSUs) containing a number of

N. R. Kim, M. W. Kim, H. J. Yoon, Prof. H. J. Choi, Prof. H.-J. Jin
Department of Polymer Science and Engineering
Inha University
Incheon 402-751, South Korea
E-mail: hjjin@inha.ac.kr

Dr. S. M. Lee, W. G. Hong, Dr. H. J. Kim
Division of Electron Microscopic Research
Korea Basic Science Institute (KBSI)
Daejeon 34133, South Korea

Prof. Y. S. Yun
Department of Chemical Engineering
Kangwon National University
Samcheok 245-711, South Korea
E-mail: ysyun@kangwon.ac.kr

DOI: 10.1002/aenm.201700629

heteroatoms; therefore, pyropolymers have properties intermediate between polymers and carbon.[27] The surface functional groups of pyropolymers are highly dependent on the polymer precursors used and the heating conditions, thereby a desirable surface property can be produced via a simple fabrication method.[27] Moreover, the highly functionalized BSUs have twisted and curved 2D-like structures with a negative curvature, exhibiting poor stacking and ordering behavior.[28,29] Hence, through controlled activation using alkali agents such as NaOH or KOH, the pore structure and specific surface area of pyropolymers are tunable and their production can be easily scaled-up.

In this study, hierarchically nanoporous pyropolymers (HN-PPs) including numerous oxygen and nitrogen heteroatoms were fabricated from polyaniline nanotubes (PNTs) by heating with KOH. The HN-PPs had a specific surface area of 3042.5 ± 91.3 m^2 g^{-1}, a large number of multitiered nanopores mainly between 1 and 5 nm in diameter, and oxygen and nitrogen heteroatoms with C/O and C/N ratios of 8.9 and 29.1, respectively. In the large operating voltage window between 1 and 4.8 V (vs Li^+/Li reference), HN-PPs showed a remarkably high specific capacity of ≈460 mA h g^{-1}, the result of storing amphicharges (Li-ion and anion) through both Faradaic reactions and EDL formation. Also, the surface-driven charge storage of HN-PPs was startlingly fast and stable, maintaining specific capacities of 265, 170, and 140 mA h g^{-1} at specific currents of 10, 20, and 30 A g^{-1}, respectively, and ≈305 mA h g^{-1} after 2000 cycles at 3 A g^{-1}. Moreover, asymmetric energy storage devices (AESDs) based on commercial graphite nanosheets (GNSs)/HN-PPs exhibited exceptionally high specific energies and powers, e.g., ≈300 W h $kg_{electrode}^{-1}$ and 5080 W $kg_{electrode}^{-1}$, respectively, and steady cycling behavior beyond 2000 cycles. This report shows the optimum material design for a surface-induced Li-ion storage electrode and demonstrates their use in practical energy storage devices.

During heating, thermal scission of the linear polyaniline backbone occurs, and the molecules produced undergo a thermal transition into hexagonal carbon structures. As shown in Figure S1 (Supporting Information), pyrolyzed PNTs (P-PNTs) have a diameter of ≈500 nm and highly rough surfaces covered with fine primary nanoparticles, which is a similar morphology to their precursor materials. The unchanged morphology of P-PNTs indicates they are a char-type carbon-based material composed of randomly oriented carbon BSUs,[30] which have a large free volume between the BSU layers resulting from their twisted and crumpled shape. Activation agents such as KOH can expand the stacking distance of BSUs via two activation steps, for example, (1) carbon consumption by oxygen, followed by (2) metallic potassium penetration into graphitic layers; these induce large open surface areas on the nanometer-scale.[7,24,31] Depending on the quantity of added KOH, the overall material properties such as morphologies, microstructures, pore structures, and surface properties of the activated pyropolymers produced are dramatically changed, as shown in **Figure 1** and Figure S2 (Supporting Information). With increasing KOH, the morphologies of PNTs are initially deformed into random shapes of a few micrometers size, indicating that KOH plays a key role in the heating process. Microstructures of the pyropolymers were characterized from X-ray diffraction (XRD) patterns and Raman spectra, as shown in Figure 1a,b. The XRD pattern of P-PNTs shows a very broad graphite (002) peak at 23.5°, indicating a poor stacking ordering of carbon BSU layers (Figure 1a). The peak is further broadened by KOH activation, as shown in the XRD patterns of *activated* PNTs (A-PNTs) and HN-PPs, and

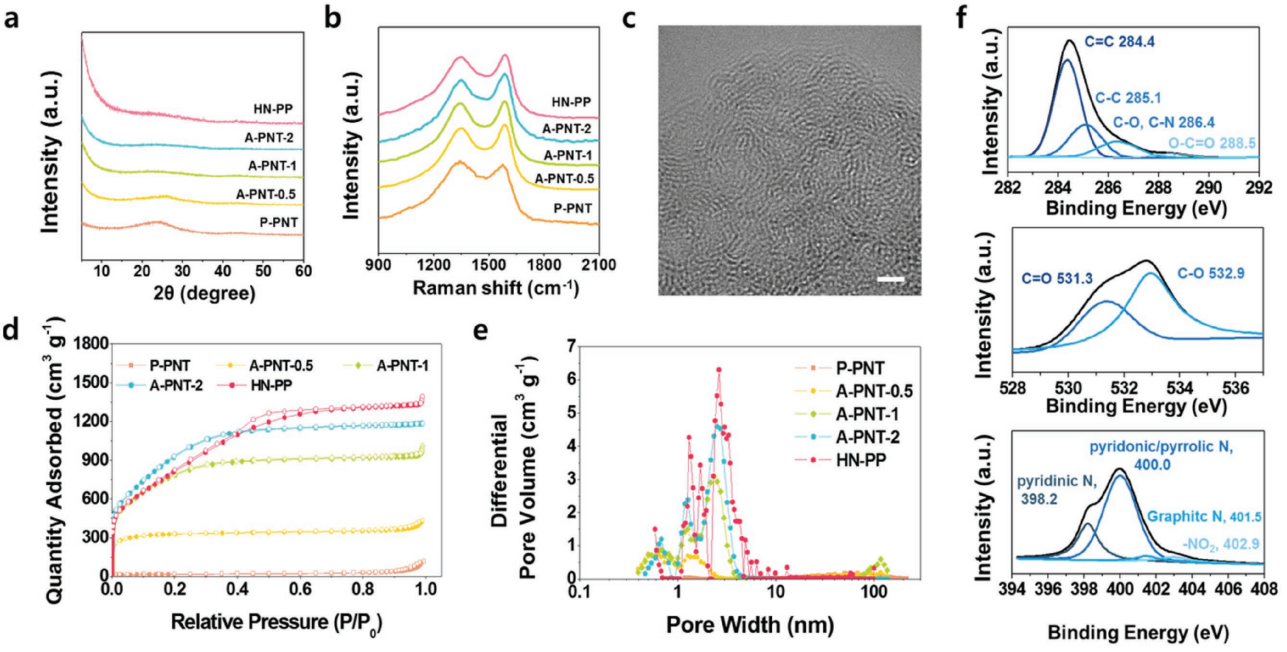

Figure 1. Materials properties of P-PNTs, A-PNTs, and HN-PPs. a) XRD patterns and b) Raman spectra of P-PNTs, A-PNTs, and HN-PPs. c) High-resolution FE-TEM image of HN-PPs. The scale bar is 2 nm. d) Nitrogen adsorption and desorption isotherm curves and e) pore size distribution data for P-PNTs, A-PNTs, and HN-PPs calculated by using the DFT model. f) XPS C 1s, O 1s, and N 1s spectra of HN-PPs.

as a result, the A-PNTs fabricated with a KOH to PNT weight ratio above 100% show no peak, indicating that they do not have a definite graphitic structure as a result of the activation. In contrast, in the low two-theta region below 10°, large intensity increases were observed with increased KOH, which occur because of a high density of nanopores formed by the activation process.[32] Raman spectra of the pyropolymers show two distinct peaks (the *D* and *G* bands) in Figure 1b. The *D* band corresponds to the disordered A_{1g} breathing mode of the hexagonal carbon structure; the *G* band originates in the six-membered aromatic ring and is related to the E_{2g} vibration mode of the sp^2-hybridized C atoms. The *D* and *G* band shapes and intensities for A-PNTs and HN-PPs are similar to each other, indicating that they have the similar carbon BSU sizes corresponding to a few nanometers. High-resolution field-emission transmission electron microscopy (FE-TEM) images of HN-PPs support the XRD and Raman spectra data (Figure 1c). It was found that there is no long-range carbon ordering, and highly disordered carbon texture is observed. However, specific pore structures and surface properties are not confirmed in the FE-TEM images; thus, materials characteristics for the A-PNTs and HN-PPs were further analyzed. Pore structures of P-PNTs, A-PNTs, and HN-PPs were characterized by nitrogen adsorption and desorption isotherm curves, as shown in Figure 1d,e. The A-PNTs show a remarkably higher quantity of adsorbed nitrogen molecules than P-PNTs (Figure 1d), indicating that KOH activation induced numerous exposed surfaces during the heating process for nitrogen adsorption. The isotherm curves exhibit three differently sloped regions: (1) a rapid increase of adsorption quantity, for relative pressure below 0.01, (2) a moderately sloped region between 0.01 and 0.6, and (3) a nearly flat region between 0.3 and 1. The first (steep) region results from monolayer adsorption/desorption of nitrogen molecules on the exposed surface area, which is the main contributor to the specific surface area of samples. The A-PNT-0.5, A-PNT-1, A-PNT-2, and HN-PP samples show a 25, 45, 50, and 45 times higher quantity of adsorbed nitrogen than the P-PNTs, in this region. The extended volume for monolayer adsorption could be induced by an increase of open surface area between carbon BSU layers, rather than by formation of additional small pores on the basal plane of the BSUs by KOH activation. Evidence for this interpretation comes from the *D* to *G* band intensity ratios in the Raman spectra, which are not critically changed in all the activated samples. Considering that nitrogen molecules have a kinetic diameter of a few tenths of a nanometer (≈0.4 nm) at low temperature, the pore size for monolayer adsorption is estimated to be on a similar sub-nanometer scale. The second diagonally sloped section of the isotherm curves indicates a continuous increase in adsorbed nitrogen, which can be explained by accumulation of additional nitrogen layers over the monolayer. This section also indicates a presence of larger pores than the first section: there is no hysteresis between the adsorption and desorption curves (except with the HN-PPs), which is a characteristic behavior of mesopores between 2 and 50 nm and originates in capillary condensation associated with pore filling by numerous nitrogen molecules. Hence, these results indicate that the A-PNTs and HN-PPs also have some nanometer pores as well as the sub-nanometer pores. Furthermore, the HN-PPs show hysteresis in the last gently sloped section, indicating the presence of mesopores. As seen in Figure 1e, the pore size distributions for A-PNTs and HN-PPs show a multimodal pore structure more clearly. It is found that several different sizes of nanopores develop below ≈5 nm, and samples with more activation exhibit a more hierarchical pore structure and larger pore volume (Figure 1e). However, when too much activation agent (above 300 wt% KOH to PNTs) is used, the carbon structures produced are highly damaged and/or decomposed; thus, a hierarchically nanoporous structure with high open surface area can be prepared by tuning the KOH contents to ≈300 wt%. In this case, the HN-PPs have a specific surface area of 3042.5 ± 91.3 m^2 g^{-1}, total pore volume of 2.12 cm^3 g^{-1}, and average pore diameter of 2.78 nm. In addition, the pore structure was characterized by means of the density functional theory (DFT) surface energy model to produce more reliable results. As shown in Figure S3 (Supporting Information), the experimental isotherms were well-matched with the DFT theoretical isotherms. Further, the specific surface areas calculated from the DFT method were generally similar to the Brunauer–Emmett–Teller (BET) specific surface areas, while slight differences were confirmed for A-PNT-1 and HN-PPs, respectively, when the DFT method was applied. This possibly resulted from the misrepresentative BET analysis of the micropores.[33] Further specific textural properties of P-PNTs, A-PNTs, and HN-PPs are presented in Tables S1 and S2 (Supporting Information).

Surface properties of HN-PPs were analyzed by X-ray photoelectron spectroscopy (XPS), as shown in Figure 1f. In the XPS C 1s spectrum, C=C (sp^2), C−C (sp^3), C−O, and C−N and C=O bonding peaks are observed at 284.4, 285.1, 286.4, and 288.5 eV, respectively (Figure 1f), which were carefully deconvoluted by referring to previous results.[34,35] The oxygen spectrum (O 1s) exhibited two different chemical bonding structures: C=O, centered at 531.3 eV; and C−O, centered at 532.9 eV (Figure 1f).[34] The nitrogen configurations (N 1s spectrum) were mainly pyridinic/pyrrolic N centered at 400.0 eV and pyridinic N centered at 398.2 eV, while minor peaks related to the N-oxide group and graphitic N were found at 402.9 and 401.5 eV, respectively.[30,34,35] For different KOH activation levels, the same oxygen and nitrogen bonding structures were also observed in the A-PNTs, as shown in Figure S4 (Supporting Information). The C/O and C/N ratios of HN-PPs were 8.9 and 29.1, respectively, indicating a higher oxygen than nitrogen content. Considering the effect of the heteroatom content and the size of the carbon BSUs in the HN-PPs, the BSU edge sites may be fully functionalized by the oxygen and nitrogen groups. In addition, the heteroatoms may have open surface exposure, providing possible contact with electrolytes. **Figure 2** presents a schematic depiction of the A-PNTs and HN-PP microstructure. A-PNTs composed of a few layers BSU stacks (pseudographitic structure) construct a dense and randomly aggregated structure of the building blocks, and HN-PPs with a poor stacking ordering of more crumpled BSU building blocks form a loosely packed structure advantageous in direct contact with an electrolyte.

Electrochemical properties of HN-PPs were characterized in an electrolyte of 1 M $LiPF_6$ in ethylene carbonate (EC)/dimethyl carbonate (DMC) within a voltage window between 1.0 and 4.8 V (vs a Li^+/Li reference). As shown in **Figure 3**a,b, cyclic voltammogram (CV) curves were tested in different voltage regions with various voltage ranges, which gives an insight into

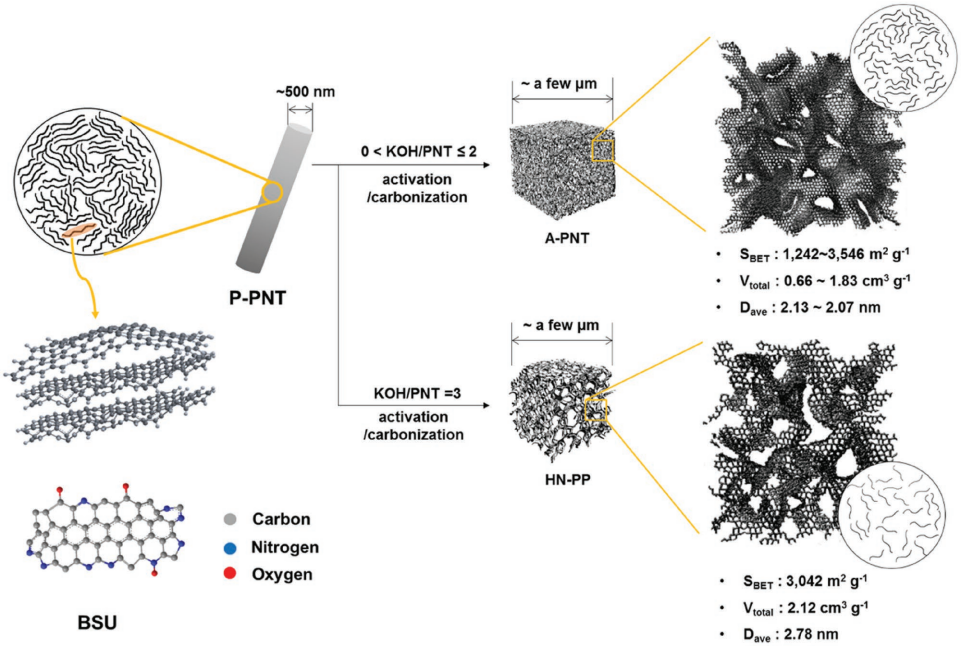

Figure 2. Schematic image exhibiting microstructures of A-PNTs and HN-PPs.

the charge storage behaviors of HN-PPs. If the charge storage mechanism is only based on ideal EDL formation, the capacitance indicated by the CV curves should be same for all the specific voltage sections and operating voltage ranges. However, in our results, the capacitances were different in the voltage regions characterized. For example, the capacitance values for 1.0–2.0 and 3.8–4.8 V voltage sections are distinctly unequal, although the voltage ranges used are the same (1 V). In the low voltage region 1.0–2.0 V (Figure 3a), the CV curve shows a specific capacitance of 92 F g^{-1}, which is the smallest capacitance for all the specific voltage regions and ranges characterized. In contrast, the CV curve in the high voltage region 3.8–4.8 V

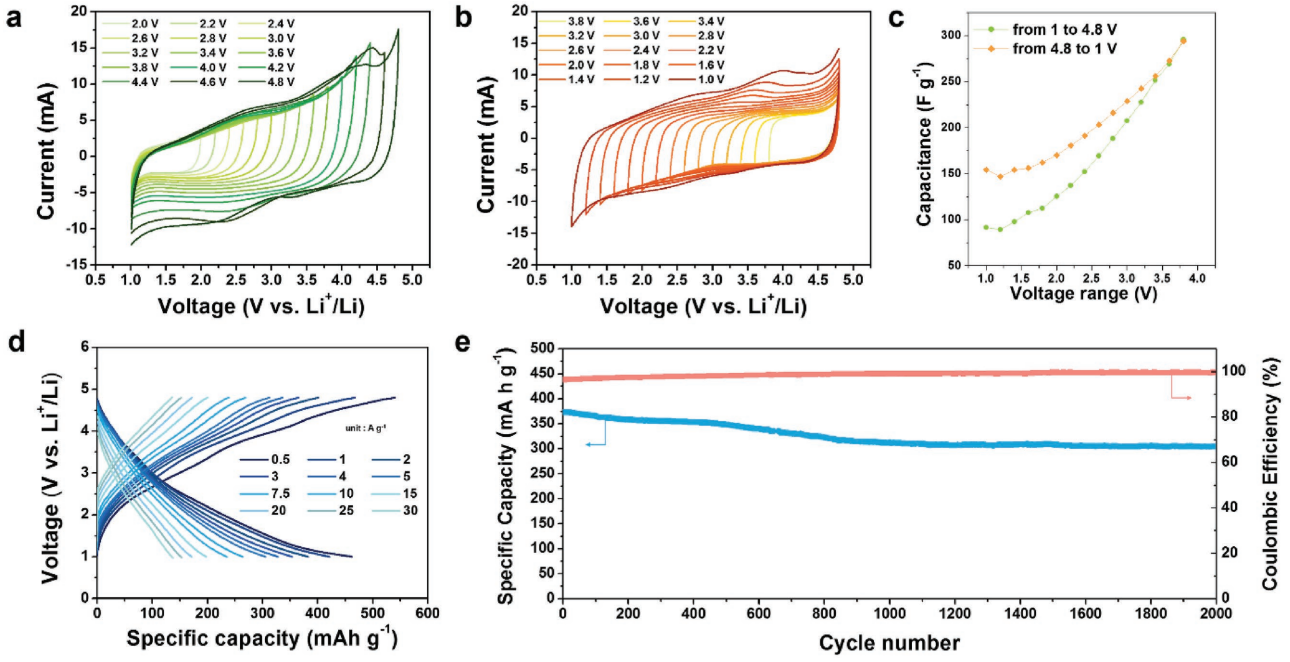

Figure 3. Electrochemical properties of HN-PPs in an electrolyte of 1 M $LiPF_6$ dissolved in EC/DMC in various voltage windows between 1.0 and 4.8 V versus Li^+/Li. CV curves at different voltage ranges a) from 1.0 to 4.8 V and b) from 4.8 to 1.0 V characterized with an interval of 0.2 V. c) Specific capacitance according to voltage section and range. d) Galvanostatic charge/discharge profiles at various current densities from 0.5 to 30 A g^{-1}. e) Cycling performance over 2000 cycles at a current density of 3 A g^{-1}.

exhibits a specific capacitance of 154 F g^{-1} (Figure 3b), which is ≈1.7 times higher than that in the voltage region 1.0–2.0 V. With an increase of the voltage ranges, the specific capacitances increase: the specific capacitances observed in the different voltage regions 1.0–3.0, 1.0–4.0, and 1.0–4.8 V are ≈125, ≈208, and ≈296 F g^{-1}, respectively (Figure 3a), and for 2.8–4.8, 1.8–4.8, and 1.0–4.8 V are ≈170, ≈229, and ≈294 F g^{-1}, respectively (Figure 3b). Further specific information for the capacitance values according to specific voltage region and voltage range can be confirmed from Table S3 (Supporting Information). The specific capacitances are remarkably dependent on not only the voltage region but also the voltage range. The capacitances characterized in the higher voltage regions are larger than those at lower voltage. And as the voltage range increases, the capacitance gap between opposite charging directions is reduced and finally reaches the same value, as shown in Figure 3c. The voltage dependency of the specific capacitances reveals a complex charge storage mechanism of HN-PPs with voltage hysteresis originating from Faradaic reactions in the numerous redox-active sites. HN-PPs provide the redox hosts for Li-ions, such as carbonyl, pyridinic, and pyridonic functional groups, however there is not redox-activity for the anion. This difference in the redox activity creates a voltage-dependent charge storage behavior. In the voltage region 1.0–3.0 V, charges may be stored mainly by redox reactions involving Li-ions at the redox-active sites, rather than by EDL formation from solvated cations. In contrast, in the voltage region 3.0–4.8 V, the solvated anions may be mainly stored by capacitive behavior rather than by the redox reaction. Nevertheless, the slopes of the log–log plotted curves exhibiting power-law relationships between sweep rates and specific currents are similar to other (≈0.91), indicating that the charge storage is mainly surface-controlled, regardless of the manner of charge storage (Figure S5, Supporting Information).[36,37] Meanwhile, the redox voltage of the pseudocapacitive reactions with Li-ions on the functional groups displays a hysteresis between charge and discharge, which limits the capacitance for smaller operating voltage ranges, because the chemical bonding formed between Li-ions and functional groups cannot then be electrochemically debonded. This issue is supported by the CV curves, as shown in Figure 3b. The CV curves in the high voltage region 3.8–4.8 V show a nearly rectangular-like shape, whereas by increasing the voltage range, the broad reduction peak is observed at around 3.5 V in 1.6–4.8 V and is shifted by ≈4 V in 1.0–4.8 V. Quasi-open circuit potential measurements demonstrate that the voltage hysteresis is of thermodynamic origin, not from kinetic polarization, as shown in Figure S6 (Supporting Information). However, with an increase of the operating voltage range, the active redox groups increase, inducing a dramatic enhancement of capacitance. When the voltage difference increases from a low voltage (1 V), the increasing capacitance ratio is higher than for the opposite case, because the chemisorption of Li-ions on the redox-active sites occurs in a relatively low voltage region (<3 V), while reversible debonding occurs at higher voltage. From these CV results, we note that: (1) capacitances originate from a number of pseudocapacitive Li-ion storage mechanisms besides EDL formation, and (2) the Faradaic reaction has a large voltage hysteresis. Therefore, the surface-induced amphicharge storage for large operating voltage ranges can improve the specific capacitance of HN-PPs by a factor of several times compared to a limited voltage range. Galvanostatic charge/discharge profiles of HN-PPs show a relationship of specific capacities versus voltage at different current rates (Figure 3d). A very high specific capacity of ≈460 mA h g^{-1} was achieved at 0.5 A g^{-1}, which is the highest value among these samples and other reported results (Figure S7, Supporting Information).[22–24] These specific capacities gradually decrease with an increase of current rate. Note that HN-PPs show high rate capabilities, in which a specific capacity of ≈140 mA h g^{-1} was maintained for a current density of 30 A g^{-1} (Figure 3d). In addition, for high loading contents of ≈10 mg cm^{-2}, high reversible capacities of ≈307 mA h g^{-1} were achieved (Figure S8, Supporting Information).[38] Furthermore, an outstanding cycling performance of over 2000 cycles is confirmed in Figure 3e. Coulombic efficiency of nearly 100% was maintained during overall cycles, and about 305 mA h g^{-1}, corresponding to 82% of the initial capacity, was attained after 2000 cycles.

To demonstrate the feasibility of HN-PPs-based energy storage devices, AESDs were assembled with commercial GNS anodes after precycling. Electrochemical performances of GNS anodes are exhibited in Figure S9 (Supporting Information), which shows a reversible capacity of ≈360 mA h g^{-1} with an average voltage of ≈0.25 V, good rate capabilities for ≈5 A g^{-1} current, and cycling performance of over 500 cycles. The initial voltages of both anode and cathode were set at 1.0 V (vs Li^+/Li) through a charge injection method,[39] and the AESDs were operated with a voltage difference 1.2–4.5 V. A schematic model for specific energy storage behavior of AESDs based on GNSs//HN-PPs is depicted in Figure S10 (Supporting Information). The asymmetric configuration of the GNSs and HN-PPs pair has a good energy and kinetic balance, exhibiting much improved energy characteristics compared to the symmetric case. The CV curves of the AESDs characterized at different sweep rates show rectangular shapes, indicating capacitive charge storage behaviors (**Figure 4**a). In addition, the galvanostatic charge/discharge profiles of the AESDs exhibit linear shapes with a maximum reversible capacity of 98 mA h g^{-1} and an average voltage of ≈2.65 V at a current rate of 0.1 A g^{-1} (Figure 4b), corresponding to a specific energy of 265 W h kg^{-1} and a specific power of 298 W kg^{-1}. With increasing the power capability to ≈5081 W kg^{-1}, the reversible capacity gradually decreases to 210 W h kg^{-1}. These relationships between energy and power characteristics are displayed as a Ragone plot in Figure 4c. The GNSs//HN-PPs deliver much higher energy and power densities than several other types of energy storage device, such as PHPNC//TiC,[40] IEVOS//graphite,[41] ZHTP//$Li_4Ti_5O_{12}$,[42] and graphene/LTO//AC.[43] Moreover, GNSs//HN-PPs show good cycling performance with capacitance retention above 70% after 2000 cycles (Figure 4d).

In summary, hierarchically nanoporous pyropolymers were fabricated from polyaniline nanotubes by simple heating with KOH. Depending on the weight ratio of KOH to PNTs, the properties of the product materials are highly tunable, particularly in regard to pore structures. HN-PPs prepared by addition of 300 wt% KOH to PNTs have a specific surface area of 3042.5 ± 91.3 m^2 g^{-1}, a total specific pore volume of 2.12 cm^3 g^{-1}, and an average pore diameter of 2.78 nm. In addition, the HN-PPs exhibit hierarchical pore structures and numerous

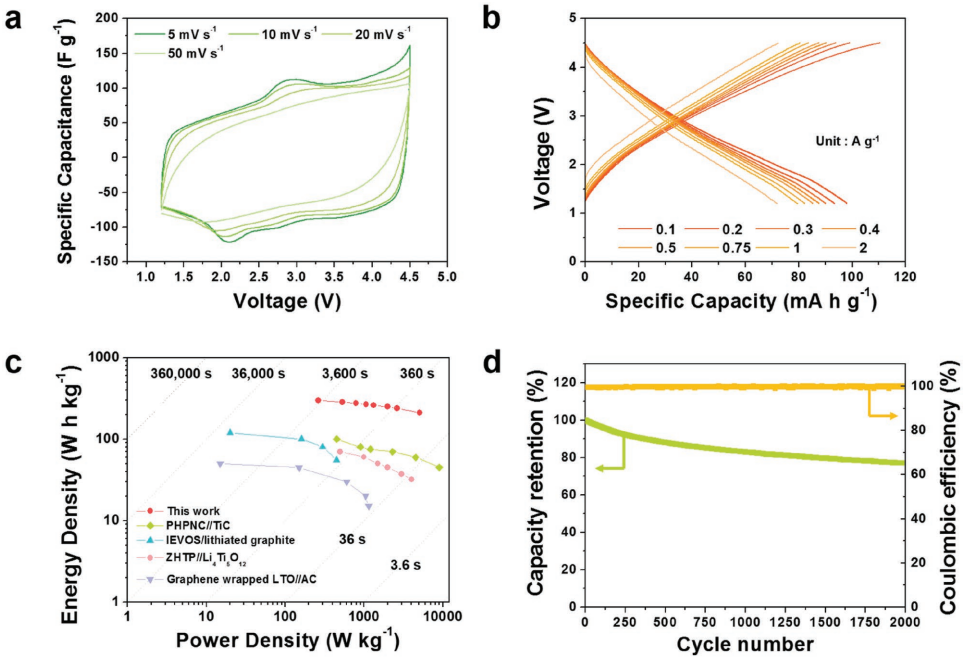

Figure 4. Electrochemical performances of AESDs based on GNSs and HN-PPs and as anodes and cathodes, respectively, in an electrolyte of 1 M $LiPF_6$ dissolved in EC/DMC in a voltage window between 1.2 and 4.5 V. a) CV curves at sweep rates of 5, 10, 20, and 50 mV s^{-1}. b) Galvanostatic charge/discharge profiles at various current densities from 0.1 to 2 A g^{-1}. c) Ragone plots of several AESDs based on GNSs//HN-PPs, PHPNC//TiC, IEVOS//lithiated graphite, ZHTP//$Li_4Ti_5O_{12}$, Graphene/LTO//AC. d) Cycling performance over 2000 cycles at a current density of 1 A g^{-1}.

redox-active oxygen and nitrogen groups (C/O and C/N ratios of 8.9 and 29.1, respectively). Charge storage behaviors of HN-PPs were characterized for different voltage regions and voltage ranges, showing that exceptionally high capacitance can be achieved in a large operating voltage window by both EDL formation and pseudocapacitive reactions of Li-ions. Specific capacities of ≈460 mA h g^{-1} and ≈140 mA h g^{-1} were attained at 0.5 and 30 A g^{-1}, and cycling stabilities were maintained over 2000 cycles, exhibiting high electrochemical performances for the HN-PPs. Moreover, AESDs based on commercial GNSs and HN-PPs as anode and cathode, respectively, delivered a high specific energy of 265 W h kg^{-1} and high specific power of 5081 W kg^{-1} with long-lasting cycling performance through 2000 cycles, demonstrating the feasibility of HN-PPs as an electrode for surface-driven energy storage.

Experimental Section

Preparation of PNTs and HN-PPs: Polyaniline nanotubes were prepared via a previously reported procedure.[44] In the fabrication process, aniline monomer (2 mmol, DC Chemical, Korea), and oxalic acid (0.5 mmol, Sigma-Aldrich) were dissolved in distilled water using a 30 min ultrasound treatment. Then, ammonium persulfate (2 mmol, Daejung Co. Ltd., Korea) which had been precooled to 4 °C was added into the reactor with stirring. After the mixture had been left for 20 h at 4 °C, the product materials were washed several times with distilled water, ethanol, and diethyl ether, then vacuum-dried at 80 °C for 24 h. The resulting PNTs were heated with KOH (weight ratios of 0%, 50%, 100%, 200%, and 300% to PNTs) to 800 °C under an Ar flow of 200 mL min^{-1}. A heating rate of 10 °C min^{-1} was applied and the final temperature held for 2 h. When a weight ratio of 300 wt% KOH to PNTs was used for the sample preparation, production of the targeted HN-PPs was achieved. Other samples were denoted as P-PNTs for 0% KOH, and A-PNTs (e.g., A-PNT-0.5, -1, and -2 for 50, 100, and 200 wt% KOH, respectively).

Characterization: Morphologies of PNTs, P-PNTs, A-PNTs, and HN-PPs were examined by field-emission scanning electron microscopy (S-4300, Hitachi, Japan) and FE-TEM (JEM2100F, JEOL, Japan). Raman spectra of the samples were recorded using a continuous-wave linearly polarized laser (514.5 nm, 2.41 eV, 16 mW). The laser beam was focused by a 100× objective lens, resulting in a spot with ≈1 µm diameter. The acquisition time and number of cycles to collect each spectrum were 10 s and 3, respectively. XRD (Rigaku DMAX 2500) analysis was performed using Cu-K_α radiation (λ = 0.154 nm) at 40 kV and 100 mA. The chemical composition of the samples was examined by XPS (PHI 5700 ESCA, USA) using monochromatic Al-K_α radiation ($h\nu$ = 1486.6 eV) and elemental analysis with an EA1112 instrument (CE Instrument, Italy). Pore structures of the samples were analyzed from nitrogen adsorption and desorption isotherms obtained using a surface area and porosimetry analyzer (Tristar, Micromeritics, USA) at −196 °C. Pore size distribution results were obtained by using the DFT model.

Electrochemical Characterization: The electrochemical properties of HN-PPs, A-PNTs, GNSs, and AESDs were characterized using a Wonatech automatic battery cycler and CR2032-type coin cells. For half-cells, coin cells were assembled in a glove box filled with argon using HN-PPs, A-PNTs, or GNSs as the working electrode and metallic Na foil as both the reference and counter electrodes. $LiPF_6$ (Aldrich, 98%) was dissolved in a solution of EC and DMC (1:1 v/v) to a concentration of 1 M and used as an electrolyte for amphiphilic charge storage. A glass microfiber filter (GF/F, Whatman) was used as a separator. Working electrodes were prepared by mixing the active material (90 wt%) with polyvinylidene difluoride (10 wt%) in *N*-methyl-2-pyrrolidone. The resulting slurries were uniformly cast on Al foil, and the resulting electrodes were dried at 120 °C for 2 h and roll-pressed. The active material mass loading was ≈1 mg cm^{-2}, and the total electrode weight was 2–3 mg. For asymmetric full cells, coin cells were assembled in a glove box under argon using HN-PPs and GNSs as the cathode and anode, respectively. The same electrolyte and separator were used, and the total electrode weight (both anode and cathode) was 4–5 mg.

For half-cells, the anode and cathode were galvanostatically cycled between 0.01 and 2.0 V (vs a Li^+/Li reference) and between 1.0 and 4.8 V (vs Li^+/Li), respectively, at various currents. In addition, AESDs were galvanostatically cycled between 1.2 and 4.5 V. To assemble the AESDs, GNSs, and HN-PPs were precycled with Li metal for ten cycles, and the onset potential of both electrodes was controlled at 1.0 V (vs Li^+/Li).

Supporting Information

Supporting Information is available from the Wiley Online Library or from the author.

Acknowledgements

This research was supported by the Basic Science Research Program through the National Research Foundation of Korea (NRF) funded by the Ministry of Education (NRF-2016R1A2B4009601) and (No. 2017R1C1B1004167). This work was also supported by Industrial Strategic Technology Development Program, (Project No. 10050477, Development of separator with low thermal shrinkage and electrolyte with high ionic conductivity for Na-ion batteries) funded by the Ministry of Trade, Industry & Energy (MI, Korea).

Conflict of Interest

The authors declare no conflict of interest.

Keywords

electrodes, hierarchically porous carbon, nanoporous carbon, pyropolymer, supercapacitors

Received: March 7, 2017
Revised: March 30, 2017
Published online: June 8, 2017

[1] B. Dunn, H. Kamath, J.-M. Tarascon, *Science* **2011**, *334*, 928.
[2] Z. Yang, J. Zhang, M. C. W. Kintner-Meyer, X. Lu, D. Choi, J. P. Lemmon, J. Liu, *Chem. Rev.* **2011**, *111*, 3577.
[3] J.-S. Lee, S. T. Kim, R. Cao, N.-S. Choi, M. Liu, K. T. Lee, J. Cho, *Adv. Energy Mater.* **2011**, *1*, 34.
[4] A. C. Luntz, B. D. McCloskey, *Chem. Rev.* **2014**, *114*, 11721.
[5] P. G. Bruce, S. A. Freunberger, L. J. Hardwick, J.-M. Tarascon, *Nat. Mater.* **2012**, *11*, 19.
[6] X. Ji, L. F. Nazar, *J. Mater. Chem.* **2010**, *20*, 9821.
[7] Y. S. Yun, K.-Y. Park, B. Lee, S. Y. Cho, Y.-U. Park, S. J. Hong, B. H. Kim, H. Gwon, H. Kim, S. Lee, Y. W. Park, H.-J. Jin, K. Kang, *Adv. Mater.* **2015**, *27*, 6914.
[8] H. Kim, H. Kim, Z. Ding, M. H. Lee, K. Lim, G. Yoon, K. Kang, *Adv. Energy Mater.* **2016**, *6*, 1600943.
[9] K. Share, A. P. Cohn, R. Carter, B. Rogers, C. L. Pint, *ACS Nano* **2016**, *10*, 9738.
[10] M.-C. Lin, M. Gong, B. Lu, Y. Wu, D.-Y. Wang, M. Guan, M. Angell, C. Chen, J. Yang, B.-J. Hwang, H. Dai, *Nature* **2015**, *520*, 325.
[11] A. J. Crowe, B. M. Bartlett, *J. Mater. Chem. A* **2016**, *4*, 368.
[12] M. Park, J. Ryu, W. Wang, J. Cho, *Nat. Rev. Mater.* **2016**, *2*, 16080.
[13] M. Ulaganathan, V. Aravindan, Q. Yan, S. Madhavi, M. Skyllas-Kazacos, T. M. Lim, *Adv. Mater. Interfaces* **2016**, *3*, 1500309.
[14] P. Simon, Y. Gogotsi, *Nat. Mater.* **2008**, *7*, 845.
[15] Y. S. Yun, G. Yoon, K. Kang, H.-J. Jin, *Carbon* **2014**, *80*, 246.
[16] F. Zhang, T. Zhang, X. Yang, L. Zhang, K. Leng, Y. Huang, Y. Chen, *Energy Environ. Sci.* **2013**, *6*, 1623.
[17] C. Merlet, B. Rotenberg, P. A. Madden, P.-L. Taberna, P. Simon, Y. Gogotsi, M. Salanne, *Nat. Mater.* **2012**, *11*, 306.
[18] C. Merlet, C. Péan, B. Rotenberg, P. A. Madden, B. Daffos, P.-L. Taberna, P. Simon, *Nat. Commun.* **2013**, *4*, 2701.
[19] J. Huang, B. G. Sumpter, V. Meunier, *Angew. Chem., Int. Ed.* **2008**, *47*, 520.
[20] C. Pean, B. Daffos, B. Rotenberg, P. Levitz, M. Haefele, P.-L. Taberna, P. Simon, M. Salanne, *J. Am. Chem. Soc.* **2015**, *137*, 12627.
[21] S. Kondrat, A. Kornyshev, *J. Phys.: Condens. Matter* **2011**, *23*, 022201.
[22] S. W. Lee, N. Yabuuchi, B. M. Gallant, S. Chen, B.-S. Kim, P. T. Hammond, Y. Shao-Horn, *Nat. Nanotechnol.* **2010**, *5*, 531.
[23] H. Kim, H.-D. Lim, S.-W. Kim, J. Hong, D.-H. Seo, D.-C. Kim, S. Jeon, S. Park, K. Kang, *Sci. Rep.* **2013**, *3*, 1506.
[24] Y. S. Yun, D.-H. Kim, S. J. Hong, M. H. Park, Y. W. Park, B. H. Kim, H.-J. Jin, K. Kang, *Nanoscale* **2015**, *7*, 15051.
[25] K. Gong, F. Du, Z. Xia, M. Durstock, L. Dai, *Science* **2009**, *323*, 760.
[26] Y. S. Yun, G. Yoon, M. Park, S. Y. Cho, H.-D. Lim, H. Kim, Y. W. Park, B. H. Kim, K. Kang, H.-J. Jin, *NPG Asia Mater.* **2016**, *8*, e338.
[27] G. M. Jenkins, K. Kawamura, *Polymeric Carbons—Carbon Fibre, Glass and Char*, Cambridge University Press, London **1976**.
[28] P. J. F. Harris, A. Burian, S. Duber, *Philos. Mag. Lett.* **2000**, *80*, 381.
[29] P. J. F. Harris, , in *Chemistry and Physics of Carbon*, Vol. *28* (Ed: L. R. Radovic), Marcel Dekker Inc., New York **2003**, 1.
[30] S. Y. Cho, Y. S. Yun, S. Lee, D. Jang, K.-Y. Park, J. K. Kim, B. H. Kim, K. Kang, D. L. Kaplan, H.-J. Jin, *Nat. Commun.* **2015**, *6*, 7145.
[31] Y. S. Yun, S. Lee, N. R. Kim, M. Kang, C. Leal, K.-Y. Park, K. Kang, H.-J. Jin, *J. Power Sources* **2016**, *313*, 142.
[32] Y. S. Yun, S. Y. Cho, J. Shim, B. H. Kim, S.-J. Chang, S. J. Baek, Y. S. Huh, Y. Tak, Y. W. Park, S. Park, H.-J. Jin, *Adv. Mater.* **2013**, *25*, 1993.
[33] G. Y. Gor, M. Thommes, K. A. Cychosz, A. V. Neimark, *Carbon* **2012**, *50*, 1583.
[34] C. Reitz, B. Breitung, A. Schneider, D. Wang, M. V. D. Lehr, T. Leichtweiss, J. Janek, H. Hahn, T. Brezesinski, *ACS Appl. Mater. Interfaces* **2016**, *8*, 10274.
[35] A. Schneider, J. Janek, T. Brezesinski, *Phys. Chem. Chem. Phys.* **2017**, *19*, 8349.
[36] V. Augustyn, J. Come, M. A. Lowe, J. W. Kim, P.-L. Taberna, S. H. Tolbert, H. D. Abruña, P. Simon, B. Dunn, *Nat. Mater.* **2013**, *12*, 518.
[37] S. Y. Cho, H. J. Yoon, N. R. Kim, Y. S. Yun, H.-J. Jin, *J. Power Sources* **2016**, *329*, 536.
[38] Y. Gogotsi, P. Simon, *Science* **2011**, *334*, 917.
[39] Z. Weng, F. Li, D.-W. Wang, L. Wen, H.-M. Cheng, *Angew. Chem., Int. Ed.* **2013**, *52*, 3722.
[40] H. Wang, Y. Zhang, H. Ang, Y. Zhang, H. T. Tan, Y. Zhang, Y. Guo, J. B. Franklin, X. L. Wu, M. Srinivasan, H. J. Fan, Q. Yan, *Adv. Funct. Mater.* **2016**, *26*, 3082.
[41] N. Xu, X. Ma, M. Wang, T. Qian, J. Liang, W. Yang, Y. Wang, J. Hu, C. Yan, *Electrochim. Acta* **2016**, *203*, 171.
[42] A. Jain, V. Aravindan, S. Jayaraman, P. S. Kumar, R. Balasubramanian, S. Ramakrishna, S. Madhavi, M. P. Srinivasan, *Sci. Rep.* **2013**, *3*, 3002.
[43] H. Kim, K.-Y. Park, M.-Y. Cho, M.-H. Kim, J. Hong, S.-K. Jung, K. C. Roh, K. Kang, *ChemElectroChem* **2014**, *1*, 125.
[44] Y. S. Yun, Y. H. Kim, M. Y. Song, N. R. Kim, K. Ku, J. S. An, K. Kang, H. J. Choi, H.-J. Jin, *J. Power Sources* **2016**, *331*, 507.

